Stability limits and transformation pathways of α-quartz under high pressure

Q. Y. Hu, J.-F. Shu, W. G. Yang, C. Park, M. W. Chen, T. Fujita, H.-K. Mao, and H. W. Sheng

Phys. Rev. B **95**, 104112 — Published 31 March 2017

DOI: 10.1103/PhysRevB.95.104112

Stability limits and transformation pathways of α-quartz under high pressure

Q.Y. Hu[1,2,3], J-F. Shu[1], W.G. Yang[1,3], C. Park[3,4], M.W. Chen[5], T. Fujita[5], H-K. Mao[1,3,]* and H.W. Sheng[1,2,]*

[1]Center for High Pressure Science and Technology Advanced Research, Shanghai 201203, P.R. China

[2]Department of Physics, George Mason University, Fairfax, VA 22030, USA

[3]Geophysical Laboratory, Carnegie Institution of Washington, Washington, DC 20015, USA

[4]High Pressure Collaborative Access Team, Geophysical Laboratory, Carnegie Institution of Washington, Argonne, IL 60439, USA

[5]WPI Advanced Institute for Materials Research, Tohoku University, Sendai 980-8577, Japan

Abstract

Ubiquitous on Earth, α-quartz plays an important role in modern science and technology. However, despite extensive research in the past, the mechanism of the polymorphic transitions of α-quartz at high pressures remains poorly understood. Here, combining *in situ* single-crystal x-ray diffraction experiment and advanced *ab initio* modeling, we report two stability limits and competing transition pathways of α-quartz under high pressure. Under near-equilibrium compression conditions at room temperature, α-quartz transits to a new *P*2/*c* silica phase, via a structural intermediate. If the thermally activated transition is kinetically suppressed, the ultimate stability of α-quartz is controlled by its phonon instability and α-quartz collapses into a different crystalline phase. Our studies reveal that pressure-induced solid-state transformation of α-quartz undergoes a succession of structural stability limits due to thermodynamic and mechanical catastrophes, and exhibits a hierarchy of transition pathways contingent upon kinetic conditions.

I. Introduction

Silica is among the most common materials in nature and possesses tremendous technological importance [1-8]. A plethora of crystal structures, including crystals and amorphous solids exist in the SiO_2 system at different pressure and temperature conditions [9-14]. The ambient polymorph of silica, α-quartz, occupies roughly 12% of the earth's crust, whose high-pressure phase behavior is of fundamental interest to materials science and geoscience. For example, with its corner-linked silica-oxygen tetrahedra in a trigonal unit cell (space group $P3_121$), α-quartz is an archetypal system for studying the pressure effects on the lattice dynamics and phase transformation of tetrahedrally bonded network framework structures [15-17].

In general, the Si-O tetrahedral motifs in α-quartz undergo transitions to Si-O six-coordinated octahedral structures (stishovite) at the upper mantle of the Earth [18] and such a coordination change occurs at several tens of gigapascals under room temperature [19-25]. Over the past decades, a large body of experimental and theoretic work has attempted to shed light on the details of the transition, but often with controversial observations and explanations [13,19,23]. Pioneering energy-dispersive x-ray diffraction studies of compressed polycrystalline α-quartz showed it collapsed to an amorphous structure above 25 gigapascal (GPa) [1,26]. In ensuing experiments that allowed various compression rates, however, either poorly crystallized stishovite [2] or a monoclinic post-quartz phase [19] has been reported as high-pressure products. On the other hand, theoretical calculations based on first-principles static calculations [5,27] and classic interatomic potentials [13,23] predicted a slew of silica polymorphs. Mechanism-wise, much less is known about the phase transition of α-quartz. Phonon softening and the associated mechanical instability have been put forward to interpret the phase behavior of α-quartz [28,29]. Recently, Martonák and colleagues [23,24] employed new simulation techniques to study the transition pathways of quartz and suggested that compressed α-quartz proceed with a direct crystalline transition pathway to the stishovite structure at 15 GPa. Here, we uncover competing transition mechanisms of compressed α-quartz by employing *in situ* single-crystal x-ray diffraction experiments and *ab initio* modeling, aiming to provide a unified picture for the phase transition of α-quartz among other oxide compounds.

II. Materials and Methods

A. X-ray diffraction experiments

X-ray diffraction experiments were performed on α-quartz single crystals at 16BM-D station of High-Pressure Collaborative Access Team (HPCAT) of the Advanced Phonon Source (APS), Argonne National Laboratory (ANL). Thin-cut natural α-quartz single crystal samples (~35μm (L)×35μm (W)×10μm (T)) were loaded in Mao-Bell diamond anvil cells. The samples were loaded to DAC chambers sealed with tungsten gaskets with helium gas as the pressure medium. Diffraction patterns were collected onto a Mar 345 image plate detector at each x-ray incident angle (1^o per image) from -15^o to 15^o. An additional image scanning over the same range of scattering angle was taken to show the integrated 2D diffraction pattern. The orientation matrix and crystalline structures were calculated with the difference-vector approach, using the single crystal solving package GSE_ADA [30]. Pressure was determined by calibrating the ruby fluorescence line shift in an off-line Ruby system. The uncertainty in pressure measurements was up to ±2 GPa, derived from the pressure change within each image collection interval. For all the experimental runs, consistent diffraction patterns were reproduced at all pressures at room temperature using multiple single-crystal samples.

B. First-principles equation of state

First-principles structural optimization was performed in the framework of density functional theory (DFT) through package Quantum ESPRESSO ver. 5.0.1 [31]. The generalized gradient approximation under the Becke-Lee-Yang-Parr (BLYP) parametrization [32,33] was employed to describe the exchange-correlation functional. Norm-conserving pseudopotentials were used with 4 valence electrons for Si ($2s^22p^2$) and 6 for O atoms ($2s^22p^4$). A plane-wave basis set with kinetic energy cut-off of 200 Ry (*i.e.*, 2730 eV) was found sufficient to converge the total energy within 2.7×10^{-7} eV. Unitcells of silica polymorphs were used for EOS calculations, in which their Brillouin zones were sampled with a Monkhorst mesh of *k* points, as shown in Table 1.

Hydrostatic pressure was applied by adding pulay stress to the diagonal elements of the stress tensor. All the structures were fully relaxed (including both cell parameters and atomic positions) in *ab initio* modeling such that the force acting on each atom was less than 0.01 eV/Å. The external pressure was within 0.1 GPa difference of the pre-conveged pressure, confirming that the optimized structure has reached a local energy minimum.

C. Free energy calculation of SiO_2 polymorphs

The Gibbs free energy $G(T,P,V)$ at certain pressure, temperature and volume is described as:

$$G = U_0 + F + PV \tag{1}$$

including cohesive energy U_0, vibrational energy F, and the pressure-volume term PV. The vibrational free energy is estimated with the quasi-harmonic approximation (QHA) [34]. Under this approximation the system is equivalent to a collection of independent harmonic oscillators, establishing the quantum mechanical energy levels of the system. In the QHA, the vibrational free energy $F(T,V)$ is computed from:

$$F(T,V) = \frac{1}{2}\sum_{\mathrm{q},s} \hbar\omega(\mathrm{q},s) + k_B T \sum_{\mathrm{q},s} \ln\left\{2\sinh\frac{\hbar\omega(\mathrm{q},s)}{2k_B T}\right\} \tag{2}$$

where $\omega(\mathbf{q},\mathrm{s})$ is the phonon frequency of sth mode for a given wave vector $\mathbf{q}$; k_B is the Boltzmann constant; $\hbar$ Plank's constant and T the temperature. The pressure P is then calculated explicitly as a derivative of the free energy with respect to volume V.

$$P = -\frac{\partial(U_0+F)}{\partial V}\Big|_T \tag{3}$$

Based on our calculation of the free energy on a variety of pressures, the equation above was used to interpolate the free energy over a wide range of pressure:

$$F_i = F_{i-1} - (U_{0i} - U_{0i-1}) - P_i(V_i - V_{i-1}) \tag{4}$$

The interpolated vibrational free energy F_i was propagated from its neighboring cohesive energy U_{oi} and volume V_i with the forward Euler method.

D. *Ab initio* metadynamics modeling

Metadynamics simulations were carried out as a barrier crossing algorithm to survey the free energy landscape of the phase transition in this work [35,36]. This method of employing supercell as order parameter was proposed to study the phase transitions of crystals [37,38] and has been successfully applied to SiO_2 [23-25]. In metadynamics computer simulation, the system is described as a function of collective variables (CVs) $\boldsymbol{S}_\alpha$. The collective variables (reaction coordinates) can be one or combinations of order parameters that characterize the system in the simulation timescale of t.

It is nontrivial to choose collective variables. In general, the changes of CVs reflect the evolution of the structures during phase transformation. The number of CVs needs to be as small as possible, so as to minimize the efforts to synchronize their depositing progress where unexpected issues may occur (*e.g.* the hill surfing problems [39]). To have more control over the dynamics in the CV space, a set of auxiliary degrees of variable $\{\boldsymbol{s}_\alpha\}$ are employed with the extended Lagrangian formulation and associated with the set of CV $\{\boldsymbol{S}_\alpha\}$[40]. Each $\boldsymbol{s}_\alpha$ is coupled with one $\boldsymbol{S}_\alpha$ such that potential hills are added slowly from the bottom of free energy well. During a molecular dynamics (MD) run with the metadynamics method, the free energy is reconstructed at each metadynamics time interval by adding a history-dependent potential, which is usually the sum of repulsive Gaussian potentials hills along the trajectory of the auxiliary variables $\boldsymbol{s}_\alpha$. The reconstructed Hamiltonian is the sum of first-principles energy (H_E, the functional of electron density $\rho(\boldsymbol{r})$ and position $\boldsymbol{r}$) and the free energy from metadynamics (V_{mtd}) is defined as:

$$H(\boldsymbol{r},\rho(\boldsymbol{r}),\boldsymbol{s}_\alpha,t) = H_E(\boldsymbol{r},\rho(\boldsymbol{r})) + V_{mtd}(\boldsymbol{s}_\alpha,t) \tag{5}$$

$$V_{mtd}(\boldsymbol{s}_\alpha,t) = \sum_{t_i<t}\left[\left\{h\exp\left(-\frac{(s^i_\alpha-s_\alpha)^2}{2{\delta_s}^2}\right)\right\}\cdot G(\boldsymbol{s}_\alpha,t)\right] \tag{6}$$

where t is the simulation time, i counts the metadynamics time step (MTD), the first Gaussian has height h and width δ_s and the second Gaussian $G(\boldsymbol{s}_\alpha,t)$ is to ensure the potential hills are slowly growing and follow a reasonable dynamics [39]. In principle, our implementation of metadynamics simulation followed literature prescriptions [39-42]. In order to determine the shapes of the Gaussian functions (height h and width δ_s), we first ran MD without depositing any bias energy for each CV combination to measure the width of the free energy well. This helped us determine the unitless scaling factors α_i to synchronize all CVs:

$$\alpha_1\omega_1 = \alpha_2\omega_2 = \alpha_3\omega_3 = \cdots \tag{7}$$

where ω_i is the fluctuation range for the ith *CV*. The Gaussian width δ_s was set to be a quarter of ω_i and applied to all CV*s* by multiplying their scaling factors.

In the production runs, the potential hills were added to the history-dependent potential V_{mtd} after each MTD. Depending on the displacement of CVs, length of MTD was adjusted in range of 1500-5000 MD steps so that the following relation was satisfied at time t_i:

$$|\boldsymbol{s}_\alpha(t) - \boldsymbol{s}_\alpha(t_i)| > \frac{3}{2}\delta_s \tag{8}$$

In this study the metadynamics simulation was performed with the CPMD package (ver. 3.15.1)[43]. A 2×2×1 α-quartz supercell (36 atoms) was slowly compressed to designated pressures. The simulation system was equilibrated for 2 picoseconds (10,000 MD time-steps) at 300 K with *ab initio* MD in an NPT ensemble [44]. During the *ab initio* MD simulation, the fluctuations of fictitious electron kinetic energy were restricted by a velocities scaling in a range of ±300 K while the nuclear degree of freedom was controlled by the Nosé-Hoover chain thermostats [45].

To reveal the structural transition of α-quartz, we initially performed test runs on a variety of combinations of CVs. Firstly, the full set of lattice parameters (a,b,c,α,β,χ) were employed as the CVs. The simulation, however, was stuck at a four-coordinated state up to 300 MTDs, presumably due to the fact that the shape of the potential well along certain CV trajectory was very steep and the deposit rate on each CV was not perfectly synchronized. On the other hand, the use of Si coordination number as the CV could promote the dynamics, but the system was quickly pushed to a random six-coordinated structure. In light of this, we chose lattice variables with relatively shallower potential wells (here, cell-edge *a* and *c*) and the average coordination number of silicon as the CVs. The scaling factors (α_i) and Gaussian shape parameters (h, δ_s) for our metadynamics simulation are listed in Table 2.

E. Phonon dispersion

First-principles phonon calculations were conducted based on the same BLYP type GGA pseudopotential using the Quantum Espresso phonon code. A 3×3×3 Monkhorst-Pack mesh was adopted for all the studied phases and the structures were completely optimized with an energy convergence of 1.0×10^{-7} eV, and the force acting on each atom less than 0.01 eV/Å.

We computed the dynamical matrix on a same grid of 3×3×3 wave vector in the Brillouin zone by applying the density functional perturbation theory (DFPT). The long range dipole-dipole interaction was taken into account using the dielectric tensor. The computed LO-TO splits were found in good agreement with literature data [46]. The phonon frequencies could be calculated at any wave vector **q** by reconstructing the dynamical matrix with the Fourier interpolation method. By comparing the results between the calculated frequencies in reciprocal space and those obtained by applying Fourier interpolation, we found that the 3×3×3 wave vector grid was sufficient to produce accurate frequencies.

The purpose for phonon calculations in this work is three-fold. a) Examine the mechanical stability of the derived metastable phases. Both the necessary and sufficient condition for the mechanical stability of a crystal is the phonon stability [47,48], *i.e.*, $\boldsymbol{\omega}(\mathbf{q},\mathbf{s})^2>0$ holds for any wave vector q and vibration mode*s*. A phonon mode that has imaginary frequency, *i.e.*, $\boldsymbol{\omega}(\mathbf{q},\mathbf{s})^2<0$, will lower the energy of the system, indicating the crystal is mechanically unstable. b) The phonon vibration modes were used to estimate the Gibbs free energy of the crystals based on the quasi-harmonic approximation. c) Monitor the phonon-softening behavior of the Brillouin zone boundary of α-quartz and to examine at what pressure the phonon instability (an indicator of mechanical instability) kicks in.

F. Solid-state nudged elastic band method

The transition pathway directly connecting two silica polymorphs was studied with the nudged-elastic band (NEB) method [49]. When the initial and final states of a reaction are known, the NEB relaxes an initial path to a minimum-energy path (MEP). The structures on the transition pathway are called "replicas", where multiple replicas are initialized as the geometric intermediates. Here we used the so-called solid-state NEB (ssNEB) [50], which is suitable in dealing with phase transitions involving cell shape changes. In this method, a *Jacobian* is used to combine atomic and cell degrees of freedom so that the MEP is insensitive to the choice of unit cell size and geometry:

$$J = \Omega^{1/3} N^{1/6} \tag{9}$$

where $\boldsymbol{\Omega}$ is the volume of the unit cell and *N* is the number of atoms in the cell. It connects the strain from the cell into the same unit of atomic position, so that the changes in the configurations $\boldsymbol{\Delta}\mathbf{R}_{\mathbf{ss}}$ is formed by concatenating the strain ε and changes in atomic coordinates $\Delta\mathbf{R}$:

$$\Delta\mathbf{R}_{ss} = \{J\epsilon, \Delta\mathbf{R}\} \tag{10}$$

The ssNEB was implemented in the Vienna *Ab* Initio Simulation Package (VASP) [51], together with the Transition States Tools VASP (VTST) [50]. Full geometry optimizations were achieved on both structures. The projected augmented-waves (PAW) pseudopotentials with Perdew-Wang type GGA parameterization [52] for Si and O with a 550 eV plane basis cutoff were used in these calculations. The initial phase and the final phase were sampled with 16 replicas with equal image distances connecting the two reactant phases. We adopted a force-based quick-min optimizer [53] to find the MEP in the phase transition pathway and the force typically converged within 200 ionic steps.

III. Results

We first demonstrate how compressed α-quartz transforms under hydrostatic conditions at room temperature. In the experiment, in order to capture the most sensitive structural changes in α-quartz under pressure, single-crystal x-ray diffraction patterns were collected in a diamond anvil cell (DAC) at different pressures. We preserved our thin-cut single-crystal samples in helium pressure medium. Selected diffraction patterns on the evolution of compressed α-quartz single crystal up to 61 GPa were shown in Fig. 1. At low pressures, sharp diffraction peaks could be readily indexed to a trigonal phase with the space group $P3_121$ (Fig. 1(a)). Above 25 GPa, the intensity of α-quartz peaks was greatly lowered, while new sets of diffraction peaks appeared, labeled in red color (Fig. 1(b-d)), indicating the formation of a new phase that persisted to higher pressures. This phase was previously interpreted as quartz II [3,13] assuming a mixed tetrahedron and octahedron framework. However, our single-crystal x-ray diffractions pattern were unambiguously indexed into a monoclinic type silica phase (Fig. 1(e), space group *P*2/*c,* designated as *m*-silica) that only contains six-coordinated Si-O octahedra, which was further corroborated with metadynamics *ab initio* modeling (see below). The quartz II phase and our *P*2/*c* phase do not show identical diffraction patterns, although they share similarities (see, *e.g.*, Fig. 1 in Ref. 3). The sharp high *d*-spacing peak in Ref. 3 (at 27.4 GPa, d~3.6 $Å^{-1}$ or Q~17.5 nm-1) is absent from our single-crystal pattern (30 GPa). The *m*-silica phase with its 2×2 Si-O octahedral framework, was distinctly different from the monoclinic phase achieved by fast compression, which was reported to consist of 3×2 octahedral blocks [19]. It is worth noting that weak diffraction spots were discernable between the (011) peak from quartz and the ($\bar{1}11$) peak from *m*-silica (Fig. 1(d)). Such weak diffraction peaks stem from a structural intermediate, as suggested by our first-principles calculations. With increasing pressure, the diffraction intensity of α-quartz and the intermediate phase became gradually lowered and eventually disappeared. The original α-quartz phase completely transformed to the *m*-silica phase above 45 GPa and was stable at least up to 61 GPa. The newly found *m*-silica phase differed in structure from previously reported $CaCl_2$ [4] and α-PbO_2 [6] types of silica and was found to be energetically comparable with these competing phases in the pressure range of interest (Fig. 2).

The transition of α-quartz to the *m*-silica resulted in a large volume collapse (*e.g.*, ~17 % at 30.5 GPa) over a wide pressure range, reflected from the experimental equations of state (EOS) of compressed α-quartz and related polymorphs as shown in Fig. 3(a). Upon the appearance of high-pressure phases, the diffraction patterns became strongly broadened and the intensities were lowered by one order of magnitude, suggesting that the single crystal sample underwent severe lattice distortions under high pressures, including possible twinning or domain splitting. Such lattice distortions and long-range imperfections could help the single crystal to survive a large volume collapse. As a result, the high-pressure *m*-silica phase was badly crystallized from the sluggish transition, showing smearing diffraction spots but with distinct crystalline ordering. In previous high-pressure experiments on alpha-quartz, the pressure-induced amorphization (PIA) phenomenon was reported, which, however, could be due to the extremely low intensities of the diffraction signals of polycrystalline powder samples. Throughout our high-pressure experiments, no broad amorphous peaks from compressed single-crystal α-quartz was identified, excluding the possibility of PIA.

The driving force for the transition from α-quartz to *m*-silica was rationalized by assessing the Gibbs free energies of the phases from first-principles calculations. Our thermodynamic analysis at 300 K indicated that the free-energy crossover of the two phases occurs at 26 GPa (Fig. 3(b)), above which *m*-silica had lower Gibbs free energy and was a more thermodynamically stable phase, setting the stage for the phase transition to take place. The theoretical prediction was in excellent agreement with our experiments where the more stable *m*-silica phase only appeared at pressures above 25 GPa, signifying a thermodynamic catastrophe of α-quartz at room temperature.

While thermodynamically permissible, the actual phase transition was dictated by its kinetics to overcome local energy barriers. Here we employed *ab initio* metadynamics simulation to probe the transition pathway. The constructed free-energy surfaces at 25 and 35 GPa were shown in Fig. 4(a)&(b). Through metadynamics, we mapped out the structures of the intermediate phase and *m*-silica (Fig. 4(c) and Fig. 5), and quantified the energy barriers for the transition (Fig. 4). At 25 GPa, the energy basin of the intermediate phase was rather shallow (Fig. 4(a)), matching our x-ray diffraction experiment where its main diffraction peak was present but with a low intensity (Fig. 1(d)). The changes of free energy in the metadynamics simulation were included in Fig. 6. At 35 GPa and 300 K, the intermediate phase dwelled in a deeper energy basin (with an energy well depth of ~0.5 k_bT) on the energy landscape (Fig. 4(b)). Experimentally, diffraction signals from the intermediate phase were visible up to 45 GPa, confirming that only a small amount of intermediate phase resides in the free energy well in a wide pressure range (25-45 GPa). The lattice parameter *a* was compressed by 8.7%, while the *c* shortened by 7.0%, leading to a 10.9% volume collapse. The length of the *b*-axis of the simulation box, however, remained almost unchanged throughout the phase transition. The volume drop, achieved by the compression of the *a* and *c* axis, formed edge-sharing octahedra chains along the (100) plane of the intermediate phase (Fig. 4(c)).

With prolonged metadynamics simulation (*e.g.*, 79 metasteps at 35 GPa, Fig. 5), the system was able to escape the energy well of the transitional intermediate phase (Fig. 4(b)), and eventually transformed into *m*-silica. We stopped the metadynamics simulation when the difference in the deposited energy for the α-quartz and *m*-silica phases matched the static free-energy calculation employing the quasi-harmonic approximation. During the phase transition from the intermediate structure to the more stable *m*-silica phase, a large enthalpy drop was observed after overcoming a small free-energy barrier. Volume continued to drop by 8.7%, mainly contributed from the shortening of the *a*-axis (4.4%) and the *c*-axis (9.2%), consistent with the experimental EOS in Fig. 3(a).

The transition from α-quartz to *m*-silica calls for significant rearrangements of both cations and anions, necessitating a thermally activated process. At room temperature, the thermal energy is not enough for the system to overcome the kinetic energy barrier quickly, and consequently, compressed silica undergoes a sluggish kinetic process, evidenced by the coexistence of multiple phases over a wide pressure range. As such, the transition path featuring the intermediate phase as a mid-product is a manifestation of kinetic constraints. It is worth noting that such a phase transition does not originate from the phonon softening of α-quartz as suggested in previous studies [28,29].

Experimentally, we did not observe a reverse transition from *m*-silica to α-quartz. The main reason is due to kinetics. For first-order solid-state phase transitions, although thermodynamically permissible, the actual phase transition is controlled by kinetics that overcomes the energy-barrier, often exhibiting a large hysteresis. It took 20 GPa (25-45 GPa) in our experiment to accomplish the kinetic process from α-quartz to *m*-silica. Likewise, it would require to a large decompression pressure range to reserve the phase transition. Considering the reconstruction to *m*-silica lowered the diffraction intensity by one order of magnitude, the recovered lower-pressure α-quartz with even weaker diffraction signals will be even more difficult to detect.

Lastly, if the phase transition described above was kinetically inhibited, *e.g.*, at very low temperatures where the kinetic energy was far below the phase transition energy barrier, the α-quartz phase would be trapped in the local energy minimum of the potential well, being metastable to higher pressures. Under this condition, we demonstrate that the ultimate stability of α-quartz is controlled by phonon softening at the K point (1/3, 1/3, 0) of the Brillouin zone. The phonon dispersion curves of α-quartz were theoretically evaluated in Fig. 7. Noticeable in the phonon dispersion curves was the phonon softening of the K point with increasing pressure. The K point phonon instability was clearly seen when the pressure reached as high as 48 GPa, shown in Fig. 8(a). Above 48 GPa, the negative vibrational modes around the K point indicated that atomic vibrations along the unstable eigenvector would destabilize the α-quartz structure, leading toward the formation of a new phase without the need for thermal excitation (Fig. 8(b)). Such a transition involves short-distance atomic shuffling, as shown in Fig. 8(c), belonging to a diffusionless transformation process. The newly formed phase after lattice collapse has a *C*222 structure where anions form a close-packed *b.c.c*-like sublattice and one-third of cations occupy the tetrahedral sites of O atoms and two-thirds of the cations occupy the octahedral sites. This same post-quartz phase has been previously predicted to form [8,21,27,54], but our results reveal that this displacive phase transition occurred at a much higher pressure (above 48 GPa).

To corroborate the mechanism of phonon instability, we analyzed the energy barrier separating α-quartz and the *C*222 silica phase employing the solid-state nudged elastic band (ssNEB) method [50]. It was evident from the calculation that the free energy barrier vanished when the pressure reached the critical value between 45 and 50 GPa (Fig. 9). Such a phase transition due to lattice instability was readily observed in *ab initio* MD simulations at finite temperatures. To this end, we conducted *ab initio* MD simulation in an *NPT* ensemble (constant particle number, pressure and temperature). Pressure was gradually applied to a 2×2×1 α-quartz supercell and the tetrahedral framework was maintained up to 50 GPa, where we found edge-sharing octahedra formed along the (100) plane. The *C*222 silica phase was mechanically stable above 50 GPa, as further confirmed by first-principles phonon calculations (Supplemental Material Fig. S1 [55]). Experimentally, under the premise of hydrostatic condition, observation of this phase transition induced by phonon instability might be preempted by other transitions occurring at lower pressures and finite temperatures.

IV. Conclusions

We have demonstrated through experimentation and simulation that the densification of α-quartz follows two distinct transition pathways: a reconstructive transition from α-quartz to *m*-silica involving an intermediate phase, as opposed to a displacive transition from α-quartz to a *C*222 silica phase induced by phonon instability. We showed that the ultimate pressure limit for the existence of α-quartz is 48 GPa. The new high-pressure phases discovered in this work are among the many possible polymorphs of silica, whose polyhedra building blocks are arranged in unique patterns that would require specific pathways to achieve. Such competing mechanisms may be operative simultaneously under certain experimental conditions and may give rise to complicated phase behaviors as seen in previous experimental work. Our findings point to the fact that, analogous to the superheating limit of crystals [56], solid-state transformation under high pressure generally follows a succession of structural stability limits arising from thermodynamic, kinetic, and mechanical considerations, resulting in a hierarchy of structural transition pathways.

References

[1] R. J. Hemley, A. P. Jephcoat, H.-K. Mao, L. C. Ming, and M. H. Manghnani, Nature **334**, 52 (1988).

[2] Y. Tsuchida and T. Yagi, Nature **347**, 267 (1990).

[3] K. J. Kingma, R. J. Hemley, H.-K. Mao, and D. R. Veblen, Phys. Rev. Lett. **70**, 3927 (1993).

[4] D. Andrault, G. F. Fiquet, F. Guyot, and M. Hanfland, Science **282**, 720 (1998).

[5] D. M. Teter, R. J. Hemley, G. Kresse, and J. Hafner, Phys. Rev. Lett. **80**, 2145 (1998).

[6] M. Miyahara, S. Kaneko, E. Ohtani, T. Sakai, T. Nagase, M. Kayama, H. Nishido, and N. Hirao, Nat. Commun. **4**, 1737 (2013).

[7] A. E. Gleason *et al.*, Nature Communs. **6**, 8191 (2015).

[8] Y. Liang, C. R. Miranda, and S. Scandolo, Phys. Rev. B **92**, 134102 (2015).

[9] L. S. Dubrovinsky, S. K. Saxena, P. Lazor, R. Ahuja, O. Eriksson, J. M. Wills, and B. Johansson, Nature **388**, 362 (1997).

[10] T. G. Sharp, A. E. Goresy, B. Wopenka, and M. Chen, Science **284**, 1511 (1999).

[11] J. Badro, D. M. Teter, R. T. Downs, P. Gillet, R. J. Hemley, and J.-L. Barrat, Phys. Rev. B **56**, 5797 (1997).

[12] T. Demuth, Y. Jeanvoine, J. Hafner, and J. G. Ángyán, J. Phys. Condens. Matter **11**, 3833 (1999).

[13] C. Campañá, M. H. Müser, J. S. Tse, D. Herzbach, and P. Schöffel, Phys. Rev. B **70**, 224101 (2004).

[14] T. Tsuchiya and J. Tsuchiya, Proc. Nat. Acad. Sci. U.S.A. **108**, 1252 (2011).

[15] R. M. Hazen, R. T. Downs, and L. W. Finger, Science **272**, 1769 (1996).

[16] J. Haines, J. M. Léger, and C. Chateau, Phys. Rev. B **61**, 8701 (2000).

[17] J. Pellicer-Porres, A. M. Saitta, A. Polian, J. P. Itie, and M. Hanfland, Nat. Mater. **6**, 698 (2007).

[18] Y. Wu, Y. Fei, Z. Jin, and X. Liu, Earth and Planet. Sci. Lett. **282**, 275 (2009).

[19] J. Haines, J. M. Leger, F. Gorelli, and M. Hanfland, Phys. Rev. Lett. **87**, 155503 (2001).

[20] R. M. Wentzcovitch, C. da Silva, J. R. Chelikowsky, and N. Binggeli, Phys. Rev. Lett. **80**, 2149 (1998).

[21] L. Huang, M. Durandurdu, and J. Keiffer, Nat. Mater. **5**, 977 (2006).

[22] T. Yagi, Nat. Mater. **5**, 935 (2006).

[23] R. Martoňák, D. Donadio, A. R. Oganov, and M. Parrinello, Nat. Mater. **5**, 623 (2006).

[24] R. Martoňák, D. Donadio, A. R. Oganov, and M. Parrinello, Physical Review B **76**, 014120 (2007).

[25] Q. Y. Hu, J.-F. Shu, A. Cadien, Y. Meng, W. G. Yang, H. W. Sheng, and H.-K. Mao, Nat. Commun. **6** (2015).

[26] K. J. Kingma, C. Meade, R. J. Hemley, H.-K. Mao, and D. R. Veblen, Science **259**, 666 (1993).

[27] N. Binggeli and J. R. Chelikowsky, Nature **353**, 344 (1991).

[28] N. Binggeli and J. R. Chelikowsky, Phys. Rev. Lett. **69**, 2220 (1992).

[29] N. Choudhury and S. L. Chaplot, Phys. Rev. B **73**, 094304 (2006).

[30] P. Dera, K. Zhuravlev, V. Prakapenka, M. L. Rivers, G. J. Finkelstein, O. Grubor-Urosevic, O. Tschauner, S. M. Clark, and R. T. Downs, High Pressure Res. **33**, 466 (2013).

[31] G. Paolo *et al.*, J. Phys. Condens. Matter **21**, 395502 (2009).

[32] C. Lee, W. Yang, and R. G. Parr, Phys. Rev. B **37**, 785 (1988).

[33] A. D. Becke, J. Chem. Phys. **98**, 5648 (1993).

[34] M. T. Dove, *Introduction to lattice dynamics* (Cambridge University Press, Cambridge, 2010), pp. 64-79.

[35] A. Laio and M. Parrinello, Proc. Nat. Acad. Sci. U.S.A. **99**, 12562 (2002).

[36] A. Laio and L. G. Francesco, Rep. Prog. Phys. **71**, 126601 (2008).

[37] R. Martoňák, A. Laio, and M. Parrinello, Physical Review Letters **90**, 075503 (2003).

[38] R. Martoňák, A. Laio, M. Bernasconi, C. Ceriani, P. Raiteri, F. Zipoli, and M. Parrinello, Z. Kristallogr. Cryst. Mater. **220**, 489 (2005).

[39] B. Ensing, A. Laio, M. Parrinello, and M. L. Klein, J. Phys. Chem. B **109**, 6676 (2005).

[40] M. Iannuzzi, A. Laio, and M. Parrinello, Phys. Rev. Lett. **90**, 238302 (2003).

[41] B. Ensing, M. De Vivo, Z. Liu, P. Moore, and M. L. Klein, Acc. Chem. Res. **39**, 73 (2006).

[42] E. Schreiner, N. N. Nair, and D. Marx, J. Am. Chem. Sci. **130**, 2768 (2008).

[43] W. Andreoni and A. Curioni, Parallel Comput. **26**, 819 (2000).

[44] G. J. Martyna, D. J. Tobias, and M. L. Klein, J. Chem. Phys. **101**, 4177 (1994).

[45] G. J. Martyna, M. L. Klein, and M. Tuckerman, J. Chem. Phys. **97**, 2635 (1992).

[46] X. Gonze, D. C. Allan, and M. P. Teter, Phys. Rev. Lett. **68**, 3603 (1992).

[47] W. E and P. Ming, Arch. Rational Mech. Anal. **183**, 241 (2007).

[48] G. Grimvall, B. Magyari-Köpe, V. Ozoliņš, and K. A. Persson, Rev. Mod. Phys. **84**, 945 (2012).

[49] H. Jónsson, G. Mills, and K. W. Jacobsen, *Classical and Quantum Dynamics in Condensed Phase Simulations* (World Scientific, Singapore, 1998), pp. 385-404.
[50] D. Sheppard, P. Xiao, W. Chemelewski, D. D. Johnson, and G. Henkelman, J. Chem. Phys. **136**, 074103 (2012).
[51] G. Kresse and J. Furthmüller, Comput. Mat. Sci. **6**, 15 (1996).
[52] G. Kresse and D. Joubert, Phys. Rev. B **59**, 1758 (1999).
[53] D. Sheppard, R. Terrell, and G. Henkelman, J. Chem. Phys. **128**, 134106 (2008).
[54] J. Dong, H. Zhu, and D. Chen, Sci. Rep. **5**, 10810 (2015).
[55] See Supplemental Material at [URL] for phonon dispersion curves, crystal structures and x-ray diffraction patterns from first-principles simulation.
[56] J. L. Tallon, Nature **342**, 658 (1989).

Acknowledgement:

We thank Bjorn O. Mysen for offering single crystal quartz samples. We acknowledge help from H.P. Yan and C. Kenney-Benson in setting up the X-ray diffraction experiment. Work at GMU was partially supported by US NSF under Grant No. DMR-1611064. Work at CIW was supported by NSF Grants EAR-1345112 and EAR-1447438. HPCAT operations are supported by the DOE-NNSA under award number DE-NA0001974 and by the DOE-BES under award number DE-FG02-99ER45775, with partial instrumentation funding by the NSF. The computational work was conducted on the SR16000 supercomputing facilities of the Institute for Materials Research, Tohoku University.

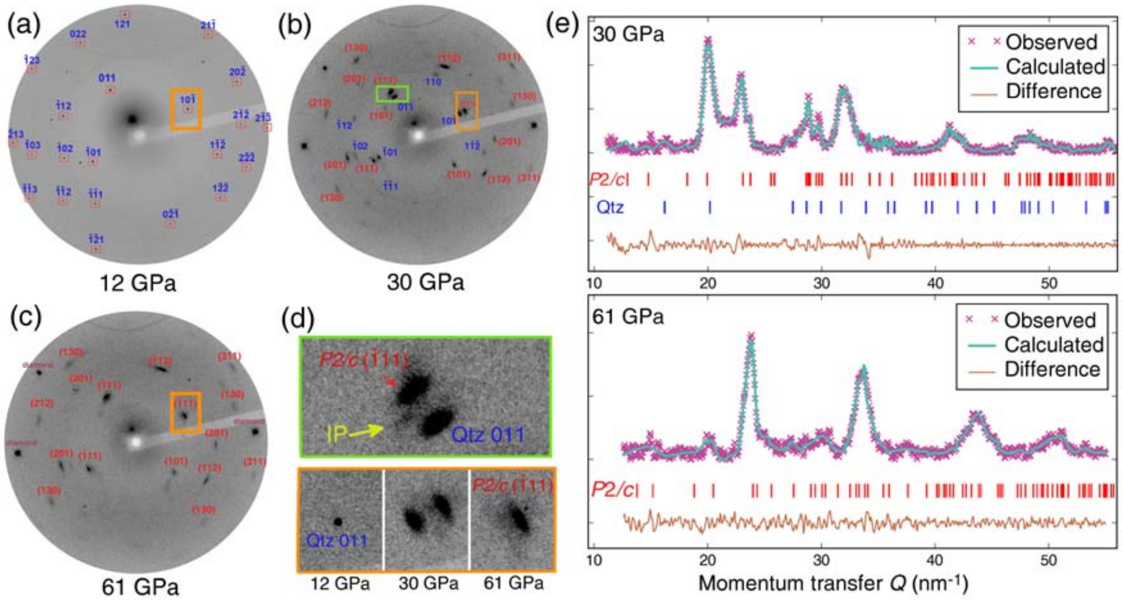

FIG. 1. Structural determination of compressed single-crystal α-quartz. (a) 2D single-crystal pattern of pure α-quartz at 12 GPa. (b) Coexistence of α-quartz and *m*-silica at 30 GPa. Red labels correspond to the emerging *m*-silica phase. The existence of the intermediate phase is marked by yellow arrows. (c) *m*-silica (space group *P*2/*c*) at 61 GPa. (d) Co-existence of three phases at 30 GPa within the green box in **b** and the evolution of single-crystal diffraction spots within the orange solid box in (a)-(c). (e) Structural refinements at 30 and 61 GPa. See Table 3 and 4 for crystallographic data. Abbreviations in the figure are: Qtz, quartz; IP, intermediate phase.

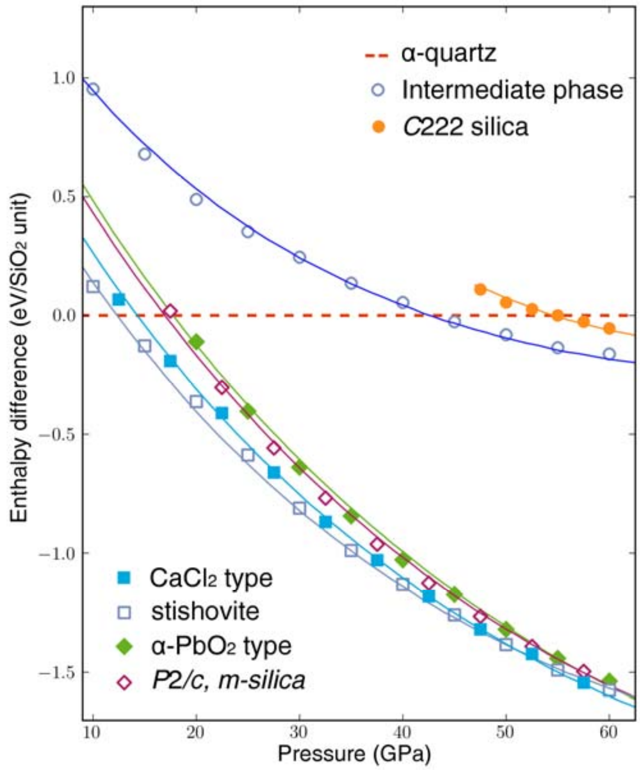

FIG. 2. Comparison of the enthalpies of seven silica polymorphs at different pressures. The enthalpies of α-quartz (space group $P3_121$), intermediate phase (*P*1), quartz III (space group *C*222), monoclinic post-stishovite (space group *P*2/*c*), stishovite (space group $P4_2/mnm$), $CaCl_2$-type post-stishovite (space group *Pnnm*) [4], and α-PbO_2-type post-stishovite (space group *Pbcn*) [6] are presented with reference to α-quartz. The solid lines are based on the fit to the calculated data with the third-order Birch-Murnaghan equation.

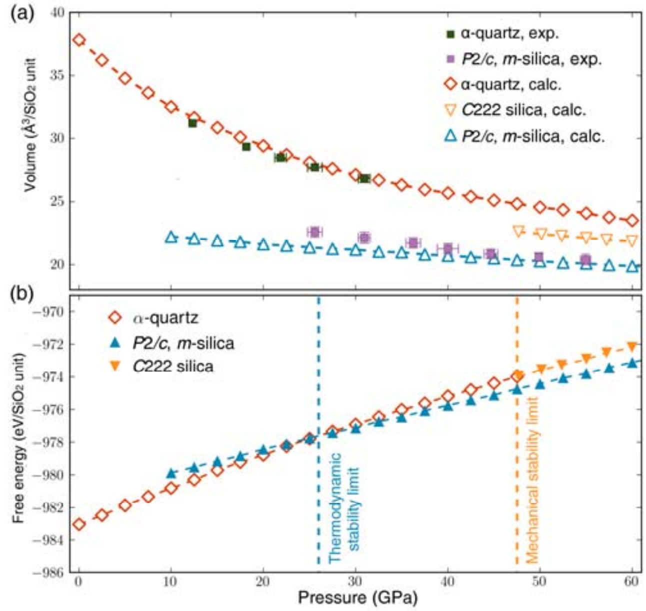

FIG. 3. Structural stability of α-quartz under high pressure. (a) Experimental and simulated EOS's of α-quartz and its polymorphs. The transition from α-quartz to *m*-silica occurs at ~ 25 GPa. (b) Calculated pressure dependence of the Gibbs free energy for α-quartz, *C*222 silica and *m*-silica based on the quasi-harmonic approximation at 300 K.

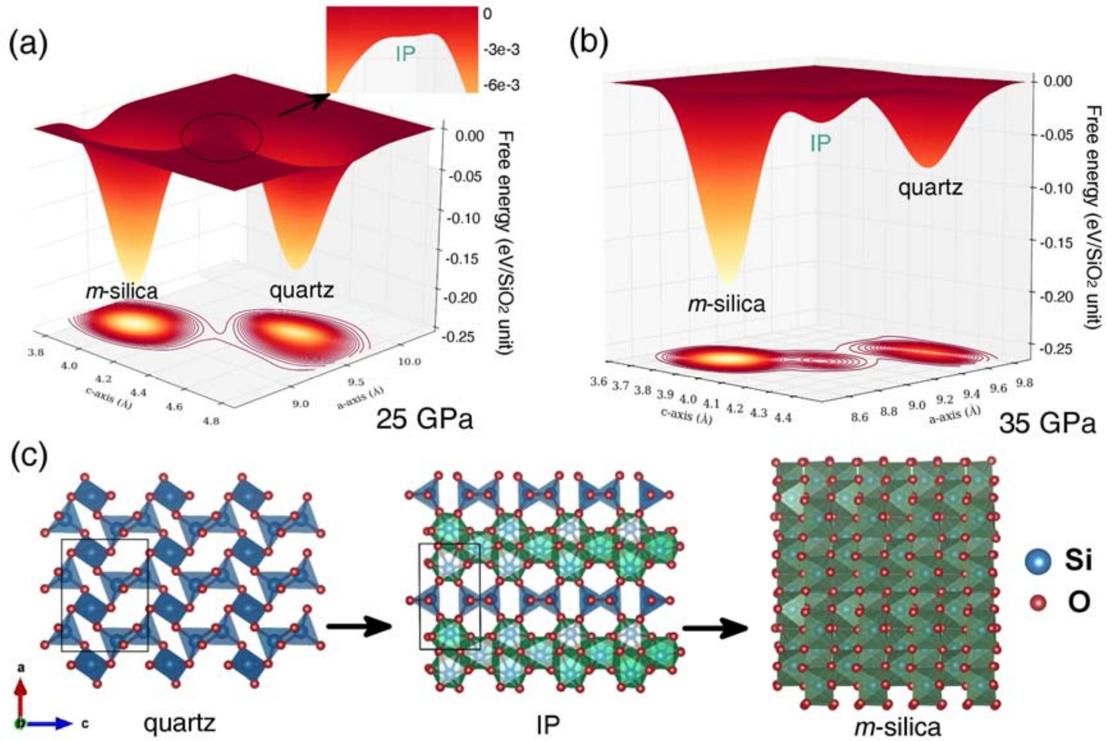

FIG. 4. Reconstructed free-energy landscape obtained from *ab* initio metadynamics simulation at (a) 25 GPa and (b) 35 GPa, projected along the *a*- and *c*-axis of the SiO_2 simulation unit cell. A local energy basin corresponding to the intermediate phase (abbreviated as IP) is present between α-quartz and the *m*-phase. The inset in (a) is rescaled to show the shallow energy well of transition intermediate. Structural changes along the transition pathway are shown in (c), illustrating the formation of octahedral Si-O structural units along the (100) plane of alpha-quartz. Calculated structures and phonon dispersion curves of IP and the *m*-phase are shown in Supplemental Material Fig. S2 and S3 [55].

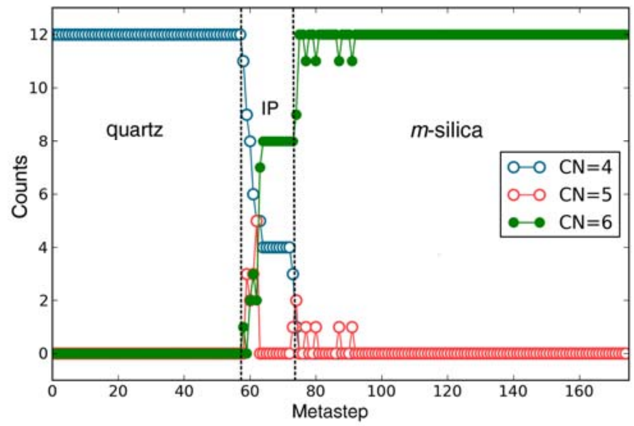

FIG. 5. Evolution of the coordination number of Si atoms along the *ab initio* metadynamics simulation of α-quartz at 35 GPa and 300 K. The bond length threshold between Si and O was set to be the distance of first peak in the radial distribution function for coordination number calculation. The oxygen atoms in the intermediate phase formed an ordered *C*2 type sublattice. With prolonged metadynamics steps, the coordination number of all Si atoms changed to six, indicating the formation of the *m*-silica phase, consistent with our experimental observations. IP: intermediate phase.

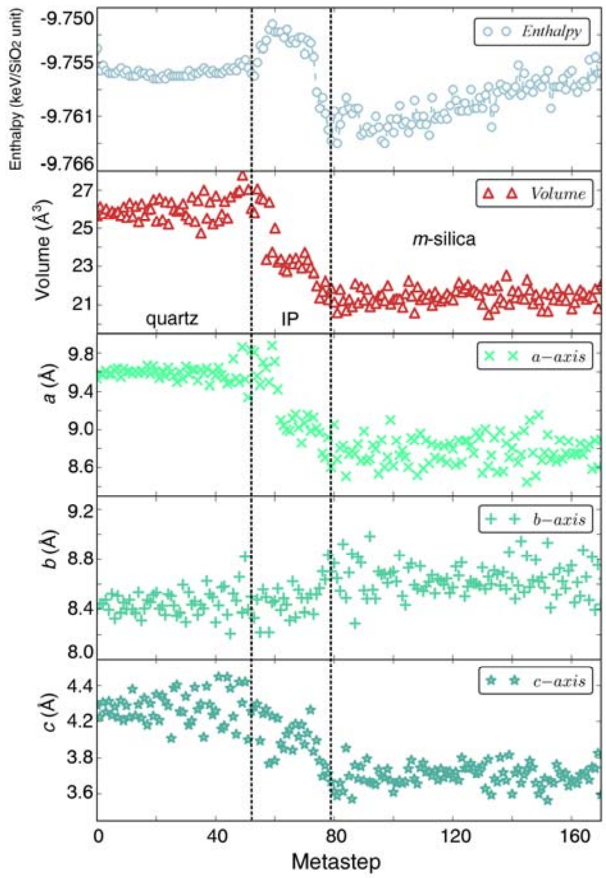

FIG. 6. Metadynamics simulation of α-quartz at 35 GPa and 300 K. The evolution of enthalpy, volume and cell parameters (starting from α-quartz) are along the *ab initio* metadynamics simulation sampling the potential energy surface. Here *a*, *b* and *c* axes refer to the three edges of the 2×2×1 simulation box. IP: Intermediate phase.

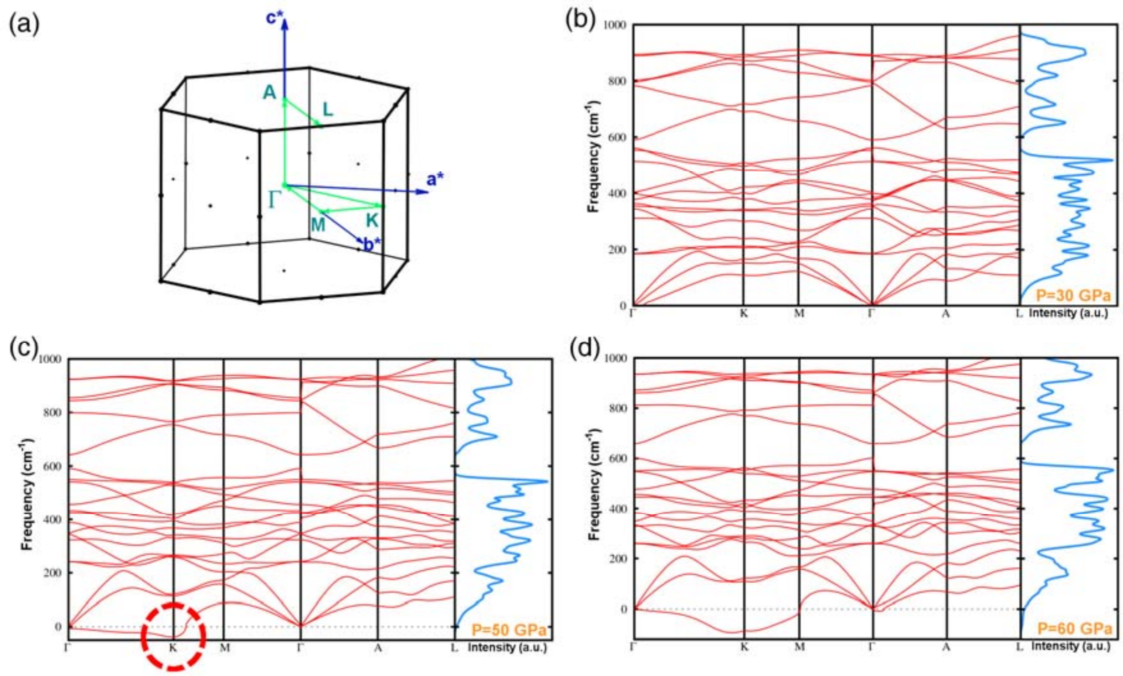

FIG. 7. Phonon softening of compressed α-quartz. (a) Sampling direction of phonon dispersion in the trigonal Brillouin zone along selected high-symmetry points. (b)-(d) Phonon dispersion curves of compressed quartz from 30-60 GPa. Γ point is the center of the Brillouin zone and other points K, M and A are located at the zone boundary. Imaginary modes are found around K point above 48 GPa, where the four coordiented Si-O sutructure units are no longer mechanically stable.

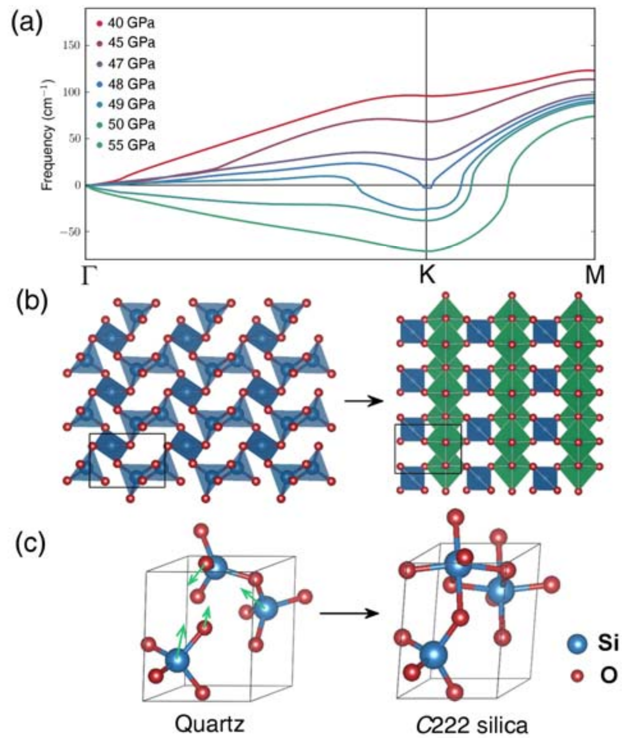

FIG. 8. Displacive transition pathway from α-quartz to *C*222 silica. (a) Phonon instability of α-quartz at the K point was observed at 48 GPa. (b) Compressed α-quartz transformed to the *C*222 silica at 50 GPa from first-principles MD. The structures were viewed along *b*-axis. The negative eigenmodes extracted from phonon analysis are visualized in (c), where the atoms of the α-quartz phase move toward the *C*222 silica structure following the unstable modes (green arrows).

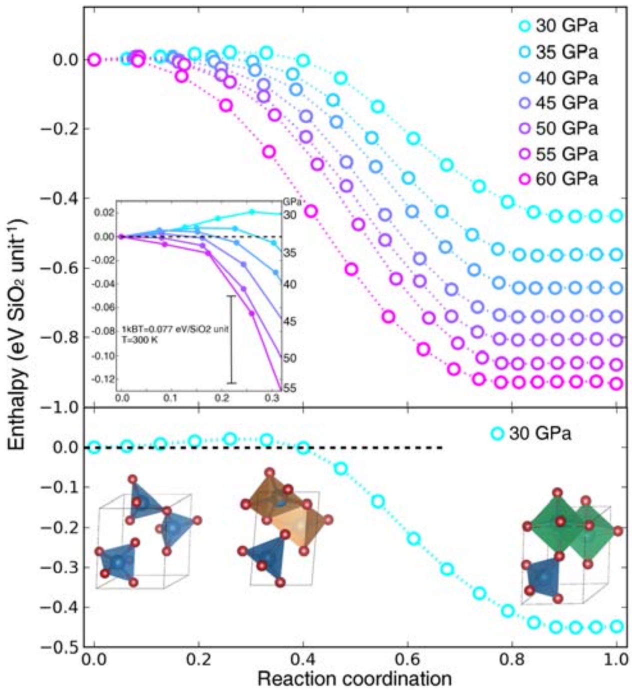

FIG. 9. The transition pathway from α-quartz to the *C*222 silica phase. Enthalpy values on the transition pathway were calculated by the ssNEB method. The inset shows the decrease of the enthalpy barrier from 30~60 GPa, where the energy barrier vanishes above 50 GPa and α-quartz spontaneously transforms to the *C*222 silica phase. The results match the phonon-instability rationale elucidated in the text. The lower panel shows the structural changes along the transition pathway. The initial and final structures are α-quartz and *C*222 silica phase, respectively. The structure taken at the saddle point of the transition path at 30 GPa shows that two thirds of the silicon atoms are five-coordinated (golden polyhedra).

Table 1. *K*-point configurations for different silica polymorphs.

silica polymorphs	Z	space group	*k-points* mesh	irreducible *k-points*
α-quartz	3	$P3_121$	3×3×3	7
Intermediate phase	12	*P*1	2×2×2	8
*C*222 silica	3	*C*222	3×3×3	14
stishovite	2	$P4_2/mnm$	5×5×5	18
$CaCl_2$ silica	2	*Pnnm*	4×4×4	30
α-PbO_2 silica	4	*Pbcn*	3×3×3	10
*P*2/*c*, *m*-silica	4	*P*2/*c*	3×3×3	14

Table 2. CV related parameters in metadynamics simulation. Here, a.u. stands for atomic unit.

P (GPa)	$\alpha_1(a)$	$\alpha_2(c)$	α_3 (coordination)	δ_s(a.u.)	$h(k_bT)$
30	3.5	4.5	2.0	0.08	1.0
35	4.0	4.0	2.0	0.06	1.0
40	4.0	4.0	2.0	0.05	1.0

Table 3. Lattice parameters and atomic coordinates of quartz obtained from the experiment (30.4 GPa) and simulation (30 GPa), respectively. The α-quartz phase reported in Figure 1 is refined by the *Rietveld* method and other phases are solved by *Le Bail* refinements. The weighted *R*-reliable factors and the χ^2-goodness of fit are *wRp*=0.132, χ^2=0.148 at 30 GPa.

	Experiment (30.4 GPa)	Simulation (30 GPa)
Z	3	3
Space group	$P3_121$	$P3_121$
a (Å)	4.359 (3)	4.314
c (Å)	5.014 (9)	5.081
V (Å^3)	82.50(14)	81.89
Si1(*x,y,z*)	0.437(8), 0.000, 0.167	0.428, 0.000, 0.167
O1 (*x,y,z*)	0.296(10), 0.303(9), 0.253(9)	0.373, 0.324, 0.251

Table 4. The *m*-silica crystal lattice at 35 GPa from experiment and simulation. The atomic positions from simulation are provided on the right.

	Experiment	Simulation	Wyckoff positions from simulation			
Z	4	4	Space group		$P2/c$	
a (Å)	4.059(4)	3.982		x	y	z
b (Å)	4.607(4)	4.574	Si1	0.000	0.152	0.250
c (Å)	4.651(8)	4.700	Si2	0.500	0.652	0.250
β	92.62(10)	91.20	O1	0.265	0.383	0.419
ρ (g/cm^{-3})	4.59(3)	4.65	O2	0.765	0.117	0.581